NOVEMBER 07 2023

Underwater acoustic sensing using the geometric phase

Trevor D. Lata; Pierre A. Deymier ; Keith Runge ; Glen S. Uehara; Todd M. W. Hodges

J. Acoust. Soc. Am. 154, 2869–2877 (2023)
https://doi.org/10.1121/10.0022322

JASA ARTICLE

Underwater acoustic sensing using the geometric phase

Trevor D. Lata,[1,a)] Pierre A. Deymier,[1,2] Keith Runge,[1,2] Glen S. Uehara,[3] and Todd M. W. Hodges[3]
[1]*Department of Materials Science and Engineering, The University of Arizona, Tucson, Arizona 85721, USA*
[2]*New Frontiers of Sound Science and Technology Center, The University of Arizona, Tucson, Arizona 85721, USA*
[3]*General Dynamics Mission Systems, 8220 East Roosevelt Street, Scottsdale, Arizona 85257, USA*

ABSTRACT:
We present a sensing modality using the geometric phase of acoustic waves propagating in an underwater environment. We experimentally investigate the effect of scattering by a small subwavelength perturbation on a flat submerged surface. We represent the state of an acoustic field in the unperturbed and perturbed cases as multidimensional vectors. The change in geometric phase is obtained by calculating the angle between those vectors. This angle represents a rotation of the state vector of the wave due to scattering by the perturbation. We perform statistical analysis to define a signal-to-noise ratio to quantify the sensitivity of the geometric phase measurement and compare it to magnitude based measurements. This geometric phase sensing modality is shown to have higher sensitivity than the magnitude based sensing approach. © *2023 Acoustical Society of America.*
https://doi.org/10.1121/10.0022322
(Received 15 June 2023; revised 8 October 2023; accepted 11 October 2023; published online 7 November 2023)
[Editor: Stephen P. Robinson] Pages: 2869–2877

I. INTRODUCTION

In general, using acoustic waves for sensing relies on changes in the wave attributes in response of the acoustic field supporting system or environment to a perturbation of the system or environment that supports the acoustic field. Changes in velocity, frequency, or amplitude are usually used in acoustic sensing technologies. The geometric phase of acoustic waves has hitherto been excluded from mainstream sensing approaches. Incorporating geometric phase in sensing modalities may create the new field of geometric phase acoustic sensing. Structured acoustic waves, such as spiral waves, and acoustic waves supporting orbital angular momentum,[1–4] carry phase information that can be exploited for sensing. For instance, imaging techniques have been devised using helical wave beams with phase singularity to beat the classical diffraction limit.[5–7] Phase has also been used in conjunction with other imaging methods to increase resolution and dynamic range in the form of phase coherence imaging.[8–10]

The total phase of a wave is the sum of the dynamical and geometric phases. The former relates to the time an acoustic wave takes to travel at its velocity along some path in the space it propagates. The geometric phase depends on the spatial degrees of freedom of the wave. These degrees of freedom can be simply discrete or continuous spatial coordinates, or convenient functions of these coordinates, such as plane waves, or Bloch waves in periodic media, or any other representation of the spatial distribution of the wave complex amplitude. These degrees of freedom or functions of degrees of freedom, when forming a complete basis set for the representation of an acoustic field, also constitute the basis of the wave's Hilbert space. The state of the wave may then be represented as a multi-dimensional vector in its Hilbert space. A change in geometric phase is the change in the angle the direction of the wave state vector makes in its Hilbert space upon a modification of the wave field due to some perturbation (e.g., scattering).

For this study, we use the term "sensing" to mean detecting a change in some environment. Establishing the ability of a metric to detect a simple change is the first step towards developing more sophisticated monitoring techniques. In recent studies, we showed that exploiting the sharp change in geometric phase near resonances can serve as a sensing modality for the remote, direct, and continuous monitoring of arctic forested areas using long-wavelength seismic waves.[11,12] We have also demonstrated sensing using the geometric phase of non-separable superpositions of acoustic waves, i.e., "classically entangled" elastic waves in externally driven parallel arrays of coupled one-dimensional metallic acoustic waveguides.[13] The sharp changes in geometric phase, associated with changes in superpositions, provide a very sensitive metric for detecting the presence of a mass scatterer. Finally, parametric exploration of the dynamics of an externally harmonically driven granular metamaterial leads to time-periodic sharp jumps in the geometric phase that can be exploited to realize mass sensors with sensitivity of approximately 10^{-5} times the mass of one granule.[14]

In the present paper, we extend the work on geometrical phase sensing to detection of scattering perturbations in underwater environments. We also focus on sensing subwavelength perturbations and quantifying the sensitivity of the geometric phase.

[a)]Email: tlata157@arizona.edu

II. EXPERIMENTAL SETUP AND METHODS

A. Source setup

A schematic of the experimental setup is given in Fig. 1. As a source of acoustic waves, we use a coupled array of acoustic waveguides composed of three aluminum rods elastically coupled via epoxy. The rods have a diameter of 1.27 cm and a height of 60 cm. The epoxy extends along their height up to 1.5 cm from either ends of the rods. The acoustic properties of this system have been well explored in Ref. 15. Transducers (Olympus, Waltham, MA, V133-RM) are attached to one end of the array using honey as an ultrasonic couplant. Rubber bands extending from the top of each rod into the lower gaps of the system apply a consistent pressure to the transducers. The bottom ends of the rods are submerged at a height of 5 mm into a tank of water equipped with a scanning arm (Onda, Sunnyvale, CA, AIMS III) and needle hydrophone (Onda, HNR-1000) to measure the acoustic field in the water. The tank has a width of 89 cm, length of 51 cm, and height of 58 cm. The water was filled to a height of 35 cm.

The source possesses three normal modes of longitudinal vibration: $\boldsymbol{e}_1 = \frac{1}{\sqrt{3}}\begin{pmatrix}1\\1\\1\end{pmatrix}$, $\boldsymbol{e}_2 = \frac{1}{\sqrt{2}}\begin{pmatrix}1\\0\\-1\end{pmatrix}$, and $\boldsymbol{e}_3 = \frac{1}{\sqrt{6}}\begin{pmatrix}1\\-2\\1\end{pmatrix}$. The $\boldsymbol{e}_1$ mode corresponds to the ends of the rods vibrating with the same amplitude and phase. The $\boldsymbol{e}_2$ mode results in only the two side rods vibrating with the same amplitude and a phase difference of 180° between them. For the $\boldsymbol{e}_3$ mode, the central rod vibrates with a phase difference of 180° with the two side rods and twice their amplitude. These three modes serve as a complete basis for describing the displacement at the ends of the rods.

A two-channel arbitrary function generator (BK Precision, Yorba Linda, CA, 4055B) is used to produce two pulse signals composed of 10 cycles of a 1 MHz sinusoid with a peak-to-peak amplitude of 4 V. The time between pulses was kept constant at 10 ms to allow the rods to come to rest between pulses. The outputs of the function generator are then amplified (PiezoDrive, Shortland, Australia PD200-V0,200) with a gain factor of 20 to increase the peak-to-peak amplitude of the pulse to 80 V before arriving at the transducers. Each of the three modes can be driven by adjusting the amplitudes and phase of the two signals. To excite the $\boldsymbol{e}_1$ mode, a single channel of the function generator was used for all three transducers to have the same nominal amplitude and phase. To excite the $\boldsymbol{e}_2$ mode, a starting phase of 180° was added to the second channel of the function generator and given to rod 3, whilst the first channel excited rod 1. For the $\boldsymbol{e}_3$ mode, the first channel drove rods 1 and 3 and the second channel had a peak-to-peak amplitude of 8 V (160 V after amplification), a starting phase of 180°, and excited rod 2. The source emits an acoustic field that is directional, thus limiting immediate reflections from the sides of the tank.

B. Perturbation setup

We intend to use the experimental setup described above to implement a geometric phase sensing modality to probe the sensitivity of the geometric phase to scattering by a subwavelength perturbation. For this, the coordinate system of the scanning tank had the (0,0,0) position fixed at the

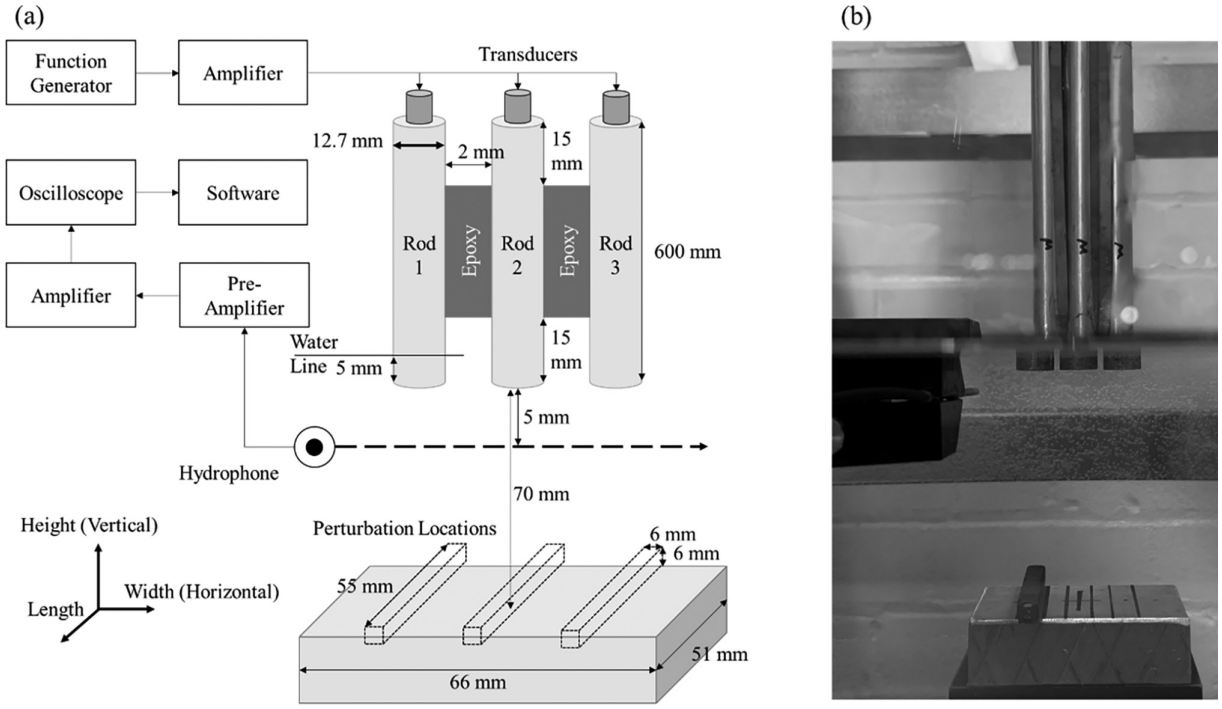

FIG. 1. (a) Diagram of experimental setup, not to scale. (b) Image of experimental setup showing the three rod source, flat reflective surface, and perturbation in the −15 mm position. The hydrophone held by the scanning arm of the tank is visible on the left side of the image.

https://doi.org/10.1121/10.0022322

center of the end of rod 2. The hydrophone is used to scan the underwater acoustic field 5 mm below the submerged ends of the rods along a horizontal direction ranging from -35 mm (left) to +35 mm (right). This scanned line is divided into 64 equidistant points. These points form a discrete set of coordinates to describe the spatial state of the acoustic wave in the vicinity of the source along the horizontal direction. The position of the axis of revolution of rods 1 and 3 along this line are −15 mm and 15 mm, respectively. We focus on sensing perturbations in echo mode, that is, we want to detect perturbations sitting on a submerged surface. To that effect, a block of aluminum was placed 70 mm away from the submerged ends of the rods that created a flat reflective surface. The block has a length of 66 mm and width of 51 mm. The flat surface is considered to be the no-perturbation case. This block produces a backscattered signal that allows us to detect, near the source, possible perturbations on the reflecting surface. For that purpose, a perturbation on the reflecting surface of the block is introduced in the form of a square steel bar with a width of 6 mm, height of 6 mm, and length 55 mm. We vary the location of this perturbation from −15, 0, and 15 mm along the horizontal direction. For both the perturbed and unperturbed situations, the surrounding environment was kept the same; thus, the only changes are the presence of the perturbation and its location. For the purposes of this paper, we are only interested in ascertaining whether the geometric phase can detect a perturbation of a given environment.

The hydrophone recorded signals pass through a preamplifier and amplifier (Onda, AH-2010-100) before arriving at an oscilloscope (Pico Technology, Tyler, TX, PicoScope 5244D). We record 500 μs of data with a sampling frequency of 25 MHz beginning with the start of the pulse in the function generator. The data are then recorded and saved using Onda's Soniq software.

C. Spectral analysis

The hydrophone records the time series of the acoustic field at the 64 discrete locations, which are Fourier transformed. The complete time series is Fourier transformed, including the incident and reflected waves. Since the Fourier transform is linear, the total frequency spectrum is the sum of the spectra of the incident part and reflected part. Indeed, let us consider the case of a source of sound emitting an acoustic pulse into an underwater environment, which results in an echo. We measure an acoustic field at n discrete points and obtain time data for each measured point and represent it as a vector $f(t) = (f_1(t), \ldots, f_n(t))$. Let us suppose we measure the field at the same points with a perturbation and represent it as $g(t) = (g_1(t), \ldots, g_n(t))$. We assume that the measured signals in $f(t)$ and $g(t)$ contain both the same incident pulse emitted by the source and an echo. These contributions add linearly and can write $f(t) = f_i(t) + f_e(t)$ and $g(t) = g_i(t) + g_e(t)$, where the subscripts i and e stand for incident and echo, respectively. The Fourier transforms of those signals are also linear combinations of the Fourier transform of the incident and echo signals, namely, $F(\omega) = F_i(\omega) + F_e(\omega)$ and $G(\omega) = G_i(\omega) + G_e(\omega)$. The incident signal is common to the perturbed and unperturbed systems. Therefore, we note that $F_i(\omega) = G_i(\omega)$ since $f_i(t) = g_i(t)$. The geometric phase in Sec. II D, which follows, will be calculated from the Fourier spectra of the complete signals. A change in the geometric phase calculated from $F(\omega)$ and $G(\omega)$ will result from the reflected part of the signal. This will enable us to avoid the difficult task of separating the reflected part from the incident part of the time series.

D. Geometric phase sensing

At each discrete location, we obtain a complex amplitude of the acoustic field in the spectral domain. At a given frequency, we represent the acoustic field as a normalized complex vector in a multidimensional Hilbert space whose 64 basis vectors correspond to locations in the physical space. This vector is illustrated as

$$s = \begin{pmatrix} a_1 \\ a_2 \\ \vdots \\ a_{63} \\ a_{64} \end{pmatrix}. \tag{1}$$

The components of this multidimensional state vector are the complex amplitudes of the field at every location in the physical space. Measuring the acoustic field at discrete points in the physical space leads to a representation with a dimension equal to the number of points. In Eq. (1), the dimension of the Hilbert space is 64. A perturbation of the physical space that scatters the acoustic wave changes the complex amplitude of the acoustic field to

$$s' = \begin{pmatrix} a'_1 \\ a'_2 \\ \vdots \\ a'_{63} \\ a'_{64} \end{pmatrix}. \tag{2}$$

This scattering results in a rotation of the normalized vector representation. The angle between the vector representation of the acoustic field along the 64 locations in the unperturbed and perturbed system corresponds to a change in the geometric phase, ϕ, of the acoustic wave. This angle is calculated from the dot product:

$$\phi = \mathrm{Sgn}(\mathrm{Im}(s^* \cdot s')) \cdot \cos^{-1}(\mathrm{Real}(s^* \cdot s')), \tag{3}$$

where s^* is the complex conjugate of s, and Im and Real stand for the imaginary and real parts of a complex quantity. The imaginary part in Eq. (3) conveys information about the sign of the change in geometric phase. So far, we illustrated the calculation of the geometric phase for 64 locations; however, this process can be applied to a subset of the 64 locations.

In that case, one considers a subspace of the complete Hilbert space with lower dimension. Considering a subspace of $q < 64$, we can define a reduced state vector without perturbation as

$$s_r = \begin{pmatrix} a_i \\ a_{i+1} \\ \vdots \\ a_{i+q-2} \\ a_{i+q-1} \end{pmatrix}. \quad (4)$$

In the presence of a perturbation, the state vector changes to s_r'. At each colocation, i, we can calculate the change in geometric phase of the reduced state vector, according to Eq. (3). Note that $i \leq 64 + 1 - q$. When the subspace is colocated with a specific physical region, started at i, the value of the change in geometric phase calculated from these reduced representations is dependent on i. Variations in the change in geometric phase of a reduced representation becomes a function of the colocation i. This approach allows us to calculate a spatial map of geometric phase change. A perturbation will rotate the colocation-dependent geometric phase of the reduced representation.

We recall that the complex amplitudes in the vectors of Eqs. (1)–(4) are obtained from the Fourier transform of the complete time series and include the incident as well as the reflected signals. As seen in Sec. II C, the incident part of the signal for the perturbed and unperturbed system are the same. A rotation of the state vector occurs only from differences in the orientation of the reflected signals. In the geometric phase sensing modality, this enables us to not rely on an arbitrary definition of a reflected signal. That is, we do not have to identify the reflected part of the time series. Moreover, the contribution to the state vector from multiple transits of the wave between the target and source will contribute less to the state vector due to attenuation of the acoustic wave.

E. Statistical analysis

For each experimental condition, we conduct ten measurements. This produces ten acoustic field state vectors for experiments with and without perturbations. The calculation of the colocation dependent change in geometric phase is performed between all pairs of perturbed and unperturbed state vectors. This results in 10×10 values of the change in geometric phase at each colocation. The average and standard deviation are calculated from these 100 values for each colocation. This is equivalent to first averaging the ten measurements for each experimental condition because we assume noise is normally distributed about zero and therefore, the expectation value and variance are linear operations. A geometric phase signal-to-noise ratio (SNR) is calculated as the absolute value of the average divided by the standard deviation. For comparison, we also calculate the difference in magnitude of the components of the state vectors of the perturbed and unperturbed systems. Again, there are 100 such differences at each point along the probed line, enabling the calculation of the average, standard deviation, and magnitude difference SNR.

III. RESULTS

A. Characterizing the source

The Fourier spectrum of the source in the absence of a perturbation calculated from the incident and reflected signals recorded underneath rod 1 is shown in Fig. 2. To test the geometric phase sensing approach, we select the frequency 144 kHz, which is common to the three modes of excitation. Waves with this frequency in the water have a wavelength of approximately 10 mm. Since the perturbation to detect has a side length of 6 mm, the wavelength of the chosen frequency is approximately two times the size of the perturbation.

We calculate the geometric phase between the acoustic fields generated when driving the $\boldsymbol{e}_1$, $\boldsymbol{e}_2$, and $\boldsymbol{e}_3$ modes to characterize how well the modes are excited. To accomplish this, we select three points directly underneath each rod's axis of revolution with which to construct a three-dimensional state vector for each mode. The geometric phases between the $\boldsymbol{e}_1$ and $\boldsymbol{e}_2$, $\boldsymbol{e}_1$, and $\boldsymbol{e}_3$, $\boldsymbol{e}_2$ and $\boldsymbol{e}_3$ modes were found to be 50.64°, –86.94°, and –40.33°, respectively. In an ideal case, the geometric phases should be 90° since the spatial modes form a complete basis for the displacement at the ends of the three rods. Phases other than 90° indicate that the source is producing a superposition of the three modes. This may be due to the difference in responses of the transducers to the same applied voltage. We also note that the transducers do not respond to all frequencies equally; this may also explain why the peak magnitude does

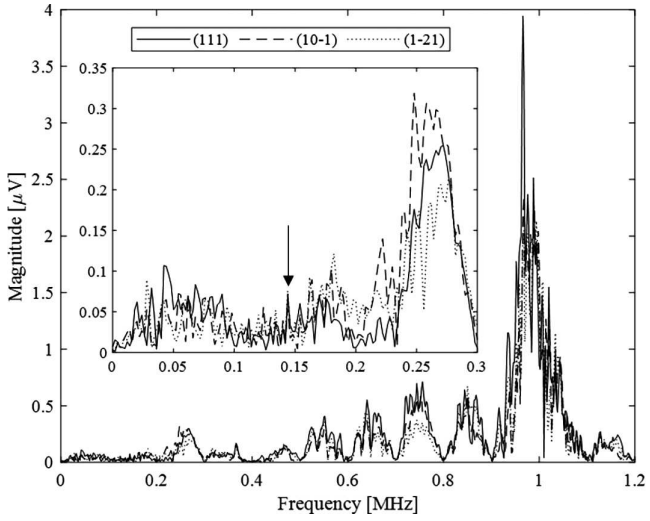

FIG. 2. Frequency spectrum obtained from the time-series data underneath the first rod when the source is excited with the $\boldsymbol{e}_1$, $\boldsymbol{e}_2$, and $\boldsymbol{e}_3$ modes. The rods are excited by a 1 MHz pulse. The pulse produces waves within a wideband of frequencies below 1 MHz. The inset shows frequencies up to 300 kHz. The regime of frequencies, where the acoustic wave has a wavelength greater than the size of the perturbation, is approximately up to 250 kHz. All three modes show comparable magnitudes at a frequency of 144 kHz (indicated by arrow).

https://doi.org/10.1121/10.0022322

not occur at 1 MHz. Using a superposition of modes is acceptable for geometric phase sensing because we are interested in the effect of perturbations on the orientation of the acoustic field state vector. The peak frequency not occurring at 1 MHz is also not important for the purposes of this paper since we confine our analysis to 144 kHz.

B. e_1 mode

In Fig. 3, we report the difference in magnitude as a function of location along the horizontal probe line for the three positions of the perturbation. The large standard deviation does not allow us to extract any spatial characteristics of the magnitude difference nor any certainty on the effect of the perturbation. We calculate a SNR, according to Sec. II E. In the three cases, the magnitude difference SNR never exceeds 2.3. Difference in magnitude is therefore a poor metric for detecting the presence of a subwavelength perturbation.

For each mode, we calculate the state vector of the perturbed and unperturbed system in a reduced Hilbert space with $q = 11$ at each colocation along the 64 point probe line. We determine the change in geometric phase between these two state vectors at each colocation. In Fig. 4, we present the average, standard deviation, and SNR in the change in geometric phase for the three positions of the perturbation.

In each case, the plots contain sections with large standard deviations but also sections with very small standard deviations. The sections with very small standard deviation correspond to a non-zero change in geometric phase. The high SNR associated with these finite changes in geometric phase provides high confidence that they result from the scattering by the subwavelength perturbation. For instance, when the perturbation is located at −15 mm, a high confidence change in geometric phase of –40° has a SNR of 4. When the perturbation is centered, we have two regions of high confidence change in geometric phase of -30° and 46° with SNR values of 5.3 and 9.2, respectively. The case of a perturbation at +15 mm gives a change in geometric phase of -26° and 42° with SNR of 3.8 and 4.1, respectively. The fact that the result for the perturbation at +15 mm is not a reflection of the result of the −15 mm case indicates that the source is not responding symmetrically. This is due to the resulting acoustic wave emitted by the rods being a superposition of the three modes, as discussed in Sec. III A. Compared to a difference in magnitude, a change in geometric phase in some regions of the colocation along the probed horizontal line can serve as a significantly better metric for the detection of the presence of a subwavelength perturbation on the reflecting surface.

To shed light on the origin of the regions with high standard deviation, we plot the individual values of the

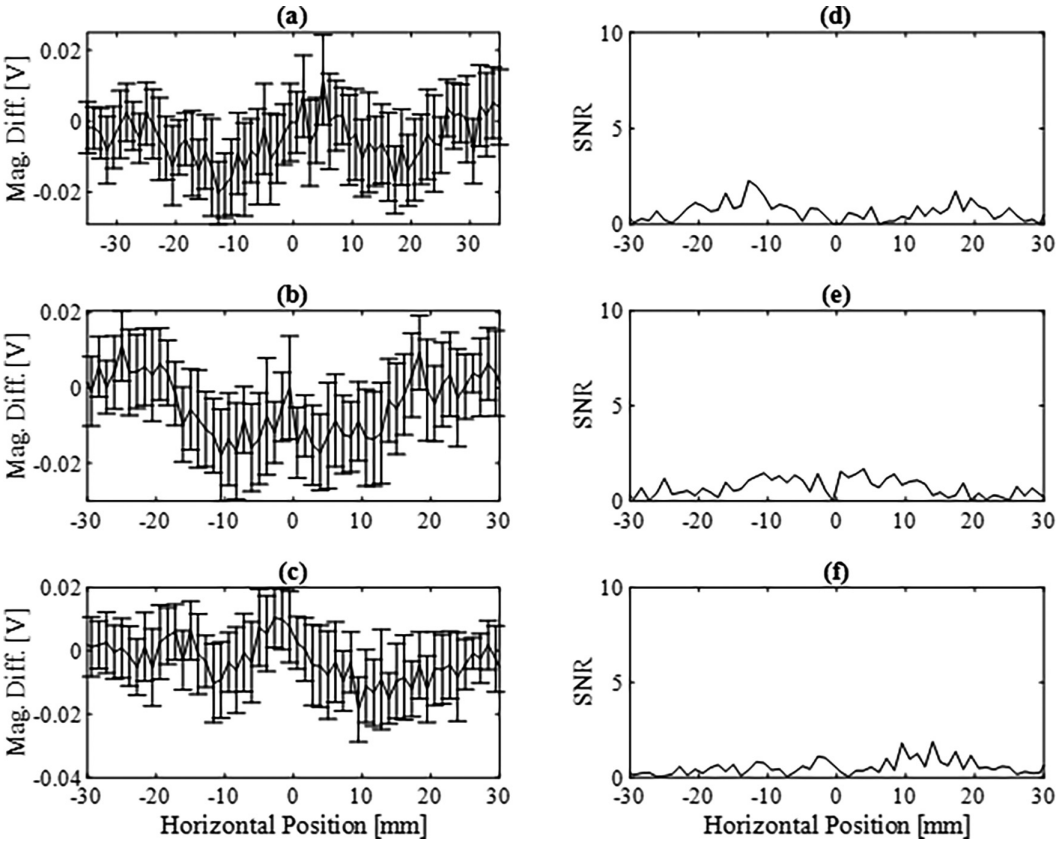

FIG. 3. (a)–(c) Average and standard deviation of the calculated difference in magnitude of the components of the acoustic field state vectors of the perturbed and unperturbed systems along the 64 points of the probed horizontal line. The perturbation is positioned at (a) –15 mm, (b) 0 mm, (c) 15 mm. (d)–(f) Magnitude difference (Mag. Diff.) SNR for the three positions of the perturbation.

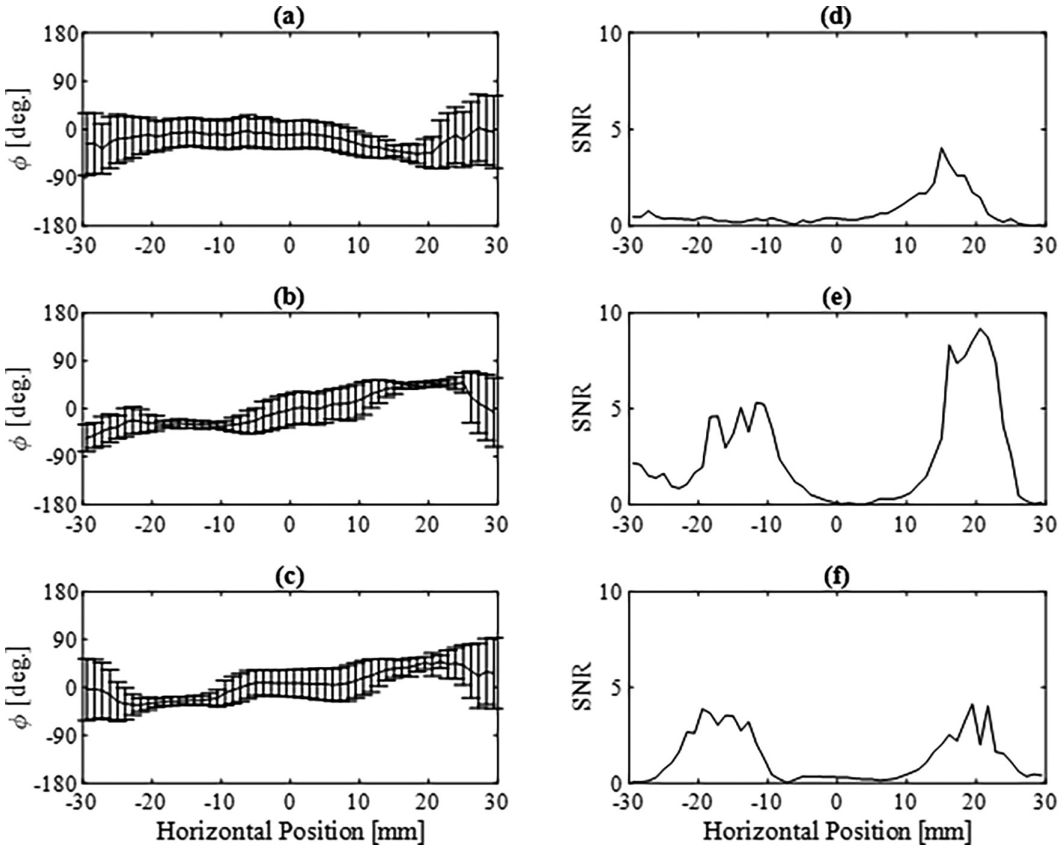

FIG. 4. (a)–(c) Change in geometric phase for the $\boldsymbol{e}_1$ mode of the measured acoustic fields with a scatterer on the left, center, and right positions, respectively. (d)–(f) Calculated SNR values for the change in geometric phase shown in the left column.

change in geometric phase as a function of the horizontal position along the probed line in Fig. 5. This figure shows clearly that the regions with high standard deviation result from bimodal distributions of the change in geometric phase. These bimodal distributions arise from the effect of the imaginary term in Eq. (3), whose sign can switch readily with small variations in the orientation of state vectors relative to each other. The switch in sign is not due to the imaginary part having a small magnitude, but because the complex inner product possesses conjugate symmetry. For example, at the horizontal position of 0 mm, there are two groups of differences in geometric phase centered on 30° and −30°. Figure 5 shows the symmetry over the entire horizontal line except the regions with high SNR. These regions reflect a nontrivial change in orientation of the acoustic field state vector due to scattering by the perturbation.

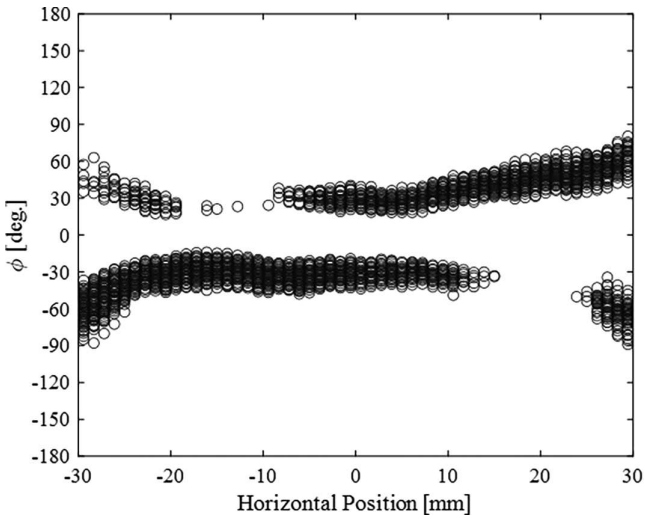

FIG. 5. Individual values of the change in geometric phase for the perturbation located in the center position for Fig. 4(b). At each colocation, there are 100 values.

C. e_2 and e_3 modes

Similar to the $\boldsymbol{e}_1$ mode, the difference in magnitude does not serve as a good metric for subwavelength detection as the maximum magnitude SNR is 1.4 for $\boldsymbol{e}_2$ (Fig. 6) and 2.2 for $\boldsymbol{e}_3$ (Fig. 7). In contrast though, the change in geometric phase (Figs. 8 and 9) exhibits features similar to those of the $\boldsymbol{e}_1$ mode. Again, the regions with high standard deviation result from bimodal distributions associated with the sign in the difference in phase. The regions of very small standard deviation correspond to changes in the phase difference amounting to tens of degrees and large SNR.

In all the geometric phase difference figures, we observe what appears to be systematic features in terms of horizontal position. These features take the form of peaks in the SNR that commonly occur around the positions of the perturbation, namely, −15, 0, and 15 mm. A systematic

https://doi.org/10.1121/10.0022322

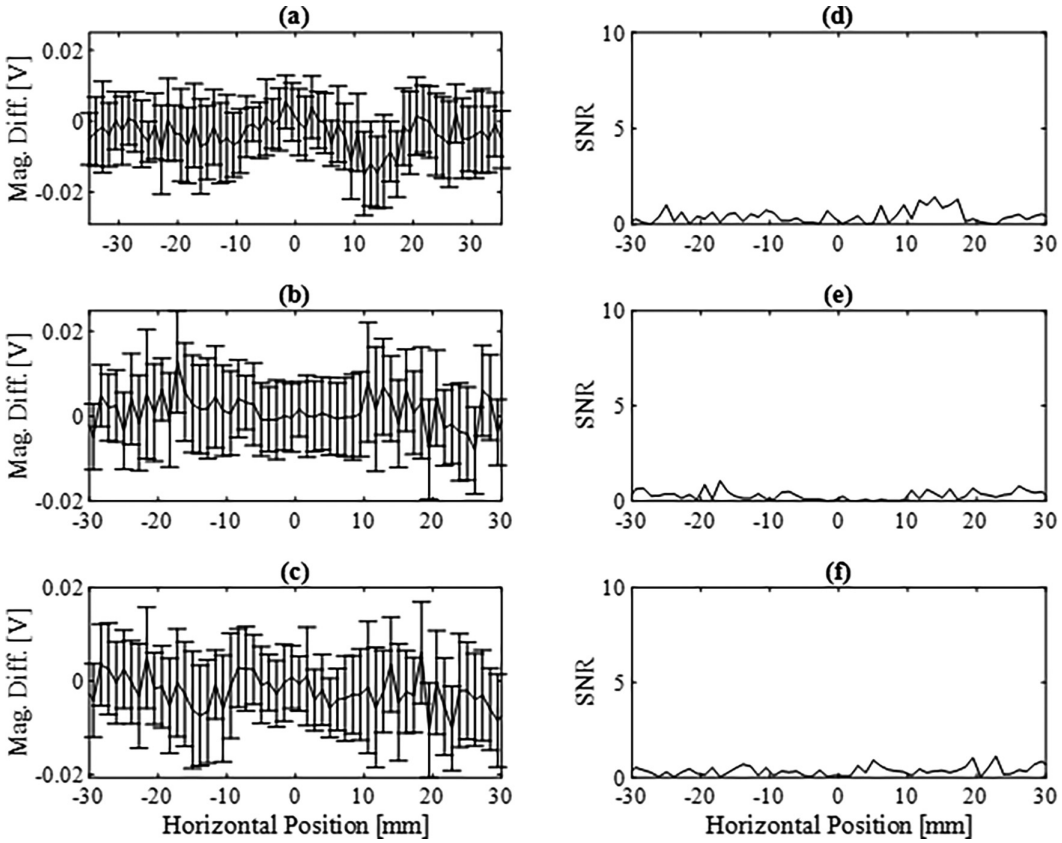

FIG. 6. Same as Fig. 3 but for the e_2 mode.

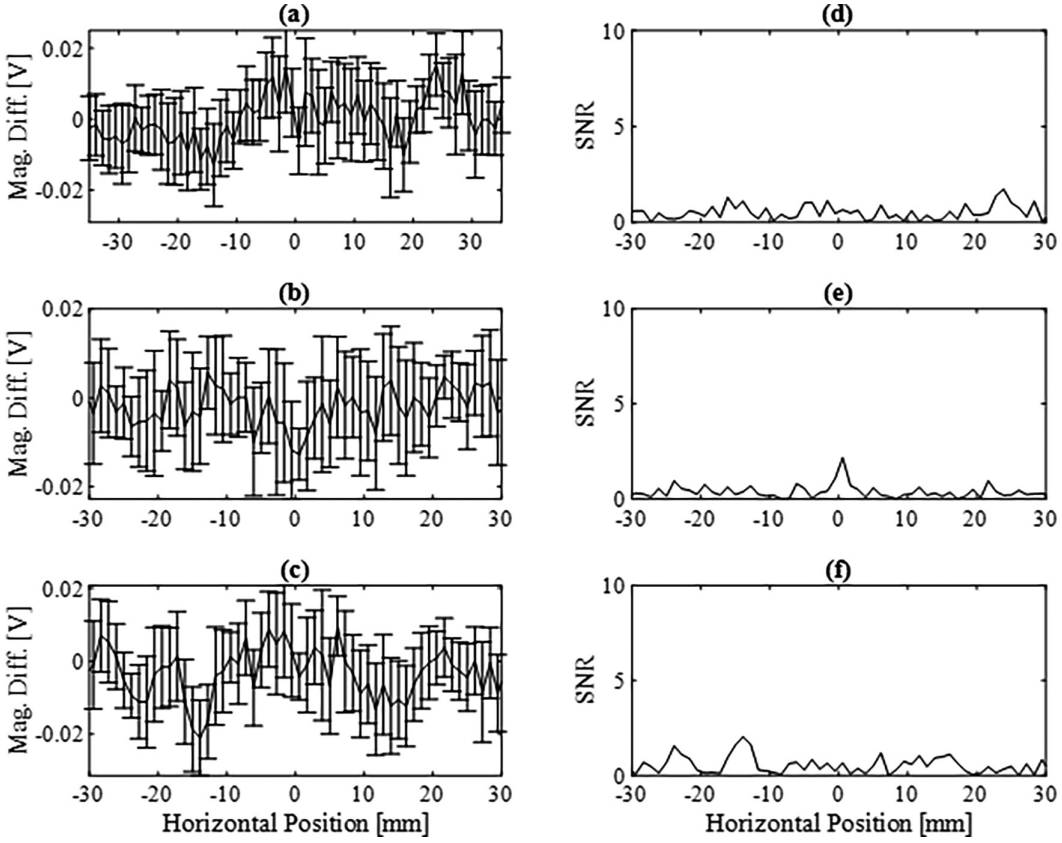

FIG. 7. Same as Fig. 3 but for the e_3 mode.

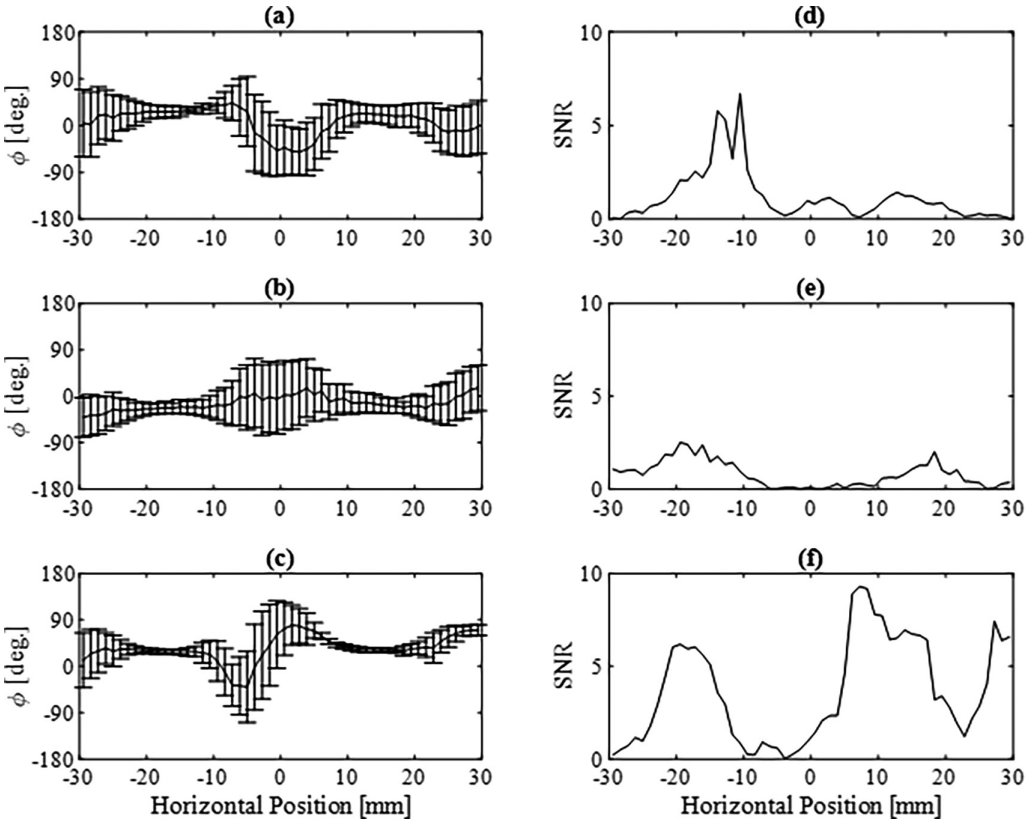

FIG. 8. Same as Fig. 4 but for the e_2 mode.

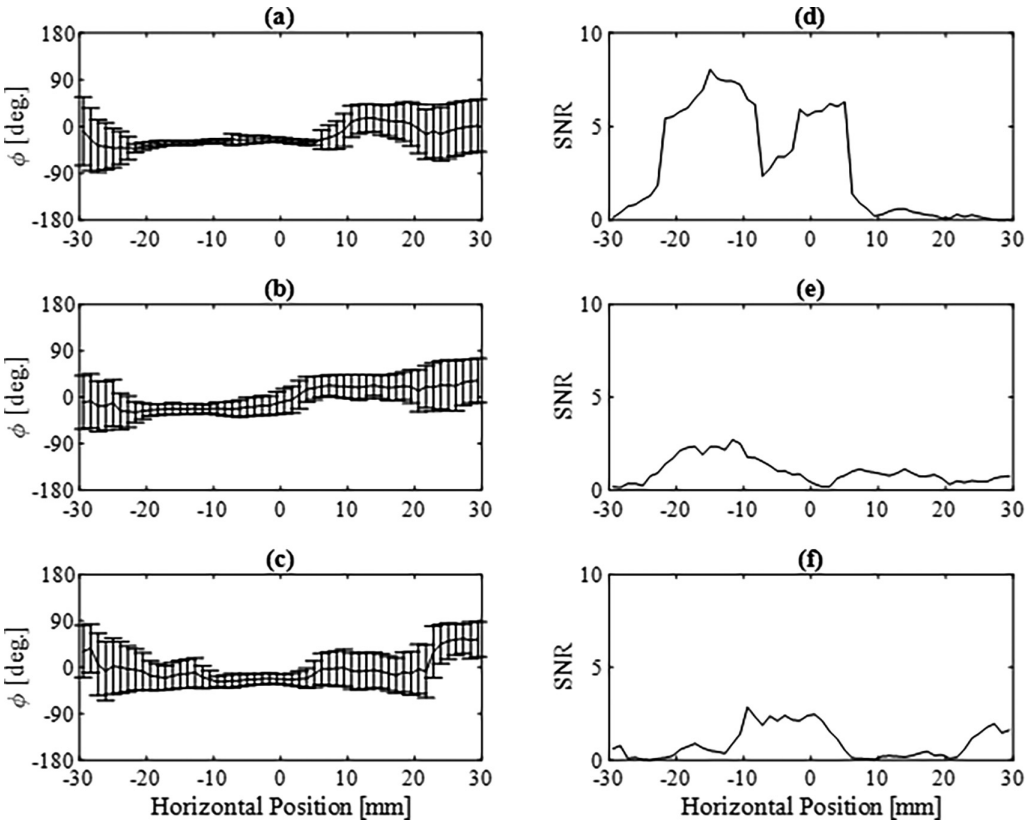

FIG. 9. Same as Fig. 4 but for the e_3 mode.

https://doi.org/10.1121/10.0022322

correlation between the position of the perturbation and the location of the peaks has yet to be identified. However, according to Fig. 4, these peaks occur where there is a gap between the positively and negatively signed phase differences. The evolution from bimodal to unimodal distributions may result from a complex interplay between the orientations of multidimensional state vectors that can be illustrated as follows. Considering the unperturbed system, we have a bundle of ten state vectors for each colocation. The orientations of these ten state vectors differ by a small amount due to experimental noise. The ten state vectors of the perturbed system have orientations differing by a small amount as well. In the multidimensional Hilbert space, the mean orientation of these two bundles could be significantly different, leading to 100 differences in geometric phase with the same magnitude and sign. In another possible case, the bundles could have a similar mean orientation while ensuring a nearly constant magnitude of the geometric phase difference between the 100 pairs of vectors. In the latter case, one would expect the calculated difference in geometric phase to have a mixture of signs.

IV. CONCLUSIONS

We have presented a possible new underwater acoustic sensing modality, based on the geometric phase of acoustic waves. This method maps a region of an acoustic field to a state vector in a multidimensional Hilbert space. By modifying the acoustic field, a local perturbation in the wave supporting medium changes the geometric phase by effectively rotating the state vector representation of the field. We use a source that supports three orthogonal spatial modes. We have shown for these modes that geometric phase sensing is sensitive to detecting the presence of a subwavelength perturbation on a reflective surface. To quantify the sensitivity of geometric phase sensing, we have compared our new approach to a method based on measuring a difference in magnitude resulting from perturbations. The magnitude difference method shows SNR of at most a value of 2, whilst changes in the geometric phase have shown regions of SNR up to a value of 10.

This work serves as a demonstration of a new underwater sensing methodology exploiting the geometric phase of acoustic waves. This geometric phase sensing modality is shown in the case of scattering by a subwavelength perturbation to have higher sensitivity than magnitude based sensing approaches. Future work will focus on extracting information on the position of the scattering perturbation. While the geometric phase sensing modality was introduced for underwater sensing, this approach is general and could be applied to high-sensitivity detection of defects or changes over wide ranges of scales in solid materials and structures as well as the natural and built environments.

ACKNOWLEDGMENTS

T.D.L., P.A.D., and K.R. are grateful for partial financial support from General Dynamics Mission Systems. This work was partially supported by the Science and Technology Center New Frontiers of Sound through National Science Foundation Grant No. 2242925.

AUTHOR DECLARATIONS

Conflict of Interest

The authors have no conflicts to disclose.

DATA AVAILABILITY

The data that support the findings of this study are available from the corresponding author upon reasonable request.

[1]B. T. Hefner and P. L. Marston, "An acoustical helicoidal wave transducer with applications for the alignment of ultrasonic and underwater systems," J. Acoust. Soc. Am. **106**, 3313–3316 (1999).
[2]J. Lekner, "Acoustic beams with angular momentum," J. Acoust. Soc. Am. **120**, 3475–3478 (2006).
[3]T. Brunet, J.-L. Thomas, R. Marchiano, and F. Coulouvrat, "Experimental observation of azimuthal shock waves on nonlinear acoustical vortices," New J. Phys. **11**, 013002 (2009).
[4]B. T. Hefner and B. R. Dzikowicz, "A spiral wave front beacon for underwater navigation: Basic concept and modeling," J. Acoust. Soc. Am. **129**, 3630–3639 (2011).
[5]T. Brunet, J.-L. Thomas, and R. Marchiano, "Transverse shift of helical beams and subdiffraction imaging," Phys. Rev. Lett. **105**, 034301 (2010).
[6]M. D. Guild, J. S. Rogers, C. A. Rohde, T. P. Martin, and G. J. Orris, "Far-field superresolution imaging using shaped acoustic vortices," in *Proc. SPIE 10600, Health Monitoring of Structural and Biological Systems XII, 1060015* (SPIE, Bellingham, WA, 2018), p. 40.
[7]M. D. Guild, C. J. Naify, T. P. Martin, C. A. Rohde, and G. J. Orris, "Superresolution using an acoustic vortex wave antenna," J. Acoust. Soc. Am. **140**, 3102 (2016).
[8]B. Gauthier, G. Painchaud-April, A. Le Duff, and P. Bélanger, "Towards an alternative to time of flight diffraction using instantaneous phase coherence imaging for characterization of crack-like defects," Sensors **21**, 730 (2021).
[9]C. Fritsch, J. Camacho, and M. Parrilla, "New ultrasound imaging techniques with phase coherence processing," Ultrasonics **50**, 122–126 (2010).
[10]J. Camacho, C. Fritsch, J. Fernandez-Cruza, and M. Parilla, "Phase coherence imaging: Principles, application, and current developments," Proc. Mtgs. Acoust. **38**, 055012 (2019).
[11]T. D. Lata, P. A. Deymier, K. Runge, F.-M. Le Tourneau, R. Ferrière, and F. Huettmann, "Topological acoustic sensing of tree spatial patterns in a model forest," Ecol. Model. **419**, 108964 (2020).
[12]T. D. Lata, P. A. Deymier, K. Runge, F.-M. L. Tourneau, R. Ferrière, and F. Huettmann, "Resonant topological acoustic sensing of permafrost thawing," Cold Reg. Sci. Tech. **199**, 103569 (2022).
[13]T. D. Lata, P. A. Deymier, K. Runge, and W. Clark, "Topological acoustic sensing using nonseparable superpositions of acoustic waves," Vibration **5**, 513–529 (2022).
[14]M. A. Hasan and P. A. Deymier, "Modelling and simulations of a nonlinear granular metamaterial: Application to geometric phase-based mass sensing," Modell. Simul. Mater. Sci. Eng. **30**, 074002 (2022).
[15]M. A. Hasan, L. Calderin, T. D. Lata, P. Lucas, K. Runge, and P. A. Deymier, "The sound of Bell states," Commun. Phys. **2**, 106 (2019).